Co-published by
Institute of Fluid-Flow Machinery
Polish Academy of Sciences
Committee on Thermodynamics and Combustion
Polish Academy of Sciences

Copyright©2026 by the Authors under licence CC BY-NC-ND 4.0

http://www.imp.gda.pl/archives-of-thermodynamics/

Enhancement of buoyancy-driven flow in an annular system by using nano-encapsulated phase change material fluid

Asmaa Nadia Bouguesri[a*], Houssem Laidoudi[b], Abderrahmane Aissa[c]

[a]Faculty of Mechanical Engineering, University of Science and Technology of Oran – Mohamed Boudiaf (USTO-MB), BP 1505, El-Menaouer, Bir El Djir 31000, Oran, Algeria
[b]Department of Mechanical Engineering, Faculty of Sciences and Technology, University of Mohamed El Bachir El Ebrahimi, El-Anasser, Bourdj Bou Arreridj 34030, Algeria
[c]Laboratoire de Physique Quantique de la Matiére et Modélisation Mathématique (LPQ3M), University of Mascara, Mascara 29000, Algeria
[*]Corresponding author email: asmaanadia.bouguesri@univ-usto.dz

Received: 02.08.2025; revised: 22.04.2026; accepted: 10.08.2026

Abstract

This study examines natural convection heat transfer in a two-dimensional annular cavity, with the inner boundary stipulated by the orthogonal intersection of two ellipses. The geometric configuration is defined by the ratio of the radii of the heated inner surface to the cooled outer cylinder such as $RR = a/r = 0.4$. The enclosure is filled with a porous medium and exposed to a uniform magnetic field, while the working fluid comprises water combined with nano-encapsulated phase change material (NEPCM) particles. The governing equations that include buoyancy effects, magnetic forces, porous medium resistance and phase-change behaviour are resolved with the Galerkin weighted residual finite element method. The flow is presumed to be steady, laminar and incompressible. A comprehensive parametric study is conducted to investigate the impact of governing physical and geometrical factors, encompassing the Rayleigh number (10^3–10^6), Hartmann number (0–80), Darcy number (10^{-5}–10^{-2}), nano-encapsulated phase change material volume fraction (0–5%), and cavity inclination angle (0°–80°). The outcomes demonstrate the progression of the flow structure, thermal field, heat transfer rate and distribution of specific heat capacity ratio within the enclosure. The elevated Ra and Da amplify convective circulation, whereas the increased Ha inhibits fluid mobility. The incorporation of nano-encapsulated phase change material markedly enhances thermal storage and mitigates temperature differences. The findings underscore the promise of NEPCM-based fluids, in conjunction with tailored cavity geometries, particularly enhancing the cross-section angles of the heated obstacle for enhanced heat management and energy-efficient mechanical system applications.

Keywords: Annular space; Natural convection; Nano-encapsulated phase change material; Heat transfer rate; Galerkin weighted residual finite element method

Vol. 47(2026), No. 3, 157–172; doi: 10.24425/ather.2026.7515

Cite this manuscript as: Bouguesri, A.N., Laidoudi, H., & Aissa, A. (2026). Enhancement of buoyancy-driven flow in an annular system by using nano-encapsulated phase change material fluid. *Archives of Thermodynamics*, 47(3), 157–172.

1. Introduction

Natural convection heat transfer is a widespread research domain owing to its fundamental relevance in manufacturing processes, like in marine engineering [1], heat exchangers [2], solar collectors [3], electronic cooling devices [4] and refrigeration systems [5], and so on. Free convection is a fundamental heat transfer mechanism, which arises from thermal gradients that create changes in fluid density, leading to the ascent of the warmer, lighter fluid and the descent of the cooler, denser fluid. The annular space with diverse cross-sectional morphologies of an interior cylinder, including circular, elliptical, and square

Nomenclature

a – major elliptical radius, m
b – minor elliptical radius, m
B_0 – magnetic flux density, T
C_p – specific heat capacity, J/(kg K)
Cr – ratio of heat capacity
Da – Darcy number
f – non-dimensional form of phase change behaviour
g – gravitational acceleration, m/s^2
h_{sf} – latent heat of the core, kJ/kg
H – aspect ratio, $H = b/a$
Ha – Hartmann number
k – thermal conductivity, W/(m K)
K_0 – permeability, m^2
L – length of the annular space, $L = r - a$, m
n, s – normal direction
N_c – suspension conductivity enhancement factor
Nu_l – local Nusselt number
$\overline{\mathrm{Nu}}$ – average Nusselt number
N_v – suspension dynamic viscosity enhancement factor
p – pressure, Pa
P – dimensionless pressure
Pr – Prandtl number
r – radius of the outer cylinder, m
Ra – Rayleigh number
RR – radii ratio, $RR = a/r$
Ste – Stefan number
T_c, T_h – cold and hot temperatures, K
T_{fu} – fusion temperature, K
T_{Mr} – temperature melting interval, K
u, v – velocity along x, and y directions, m/s
U, V – dimensionless velocity components
x, y – Cartesian coordinates, m
X, Y – dimensionless coordinates

Greek symbols

α – thermal diffusivity, m^2/s
β – thermal expansion coefficient, 1/K
ε – porosity of the porous medium
θ – dimensionless temperature
λ – dimensionless heat capacity
ι – mass ratio of the shell and core of NEPCM
μ – dynamic viscosity, kg/(s m)
ρ – density, kg/m^3
ϕ – nanoparticle volume fraction, %

Subscripts and Superscripts

b – mixture
co – core of the NEPCM
f – host fluid
p – NEPCM particle
sh – NEPCM shell

Abbreviations and Acronyms

ANN – artificial neural network
GFEM – finite element method
MHD – magnetohydrodynamic
NEPCM – nano-encapsulated phase change material
PCM – phase change material

shapes, was the focus of scientific scrutiny owing to its potential of enhancing heat transfer efficiency. The research initiatives aim to contribute to the integration of these concepts into industrial frameworks.

A considerable number of numerical and experimental studies have significantly expanded our understanding of natural convection heat transfer in circular enclosures. For example, Kuehn and colleagues [6] conducted an experimental investigation to examine the effects of eccentricity and Rayleigh number on the thermal performance of horizontal cylindrical annuli. Similarly, Wang and co-workers [7] applied a computational method based on the central difference approach and validated their results using the Mach-Zehnder interferometer in an annular configuration. In a different series of studies, Laidoudi and colleagues [8–11] performed numerous numerical analyses in cold circular enclosures containing one or more hot concentric internal cylinders arranged in various configurations. Helmaoui et al. [12] investigated the effect of a pair of heated semi-circular tubes, while Khudhair et al. [13] demonstrated that vibration enhances heat transfer in annular spaces at low Rayleigh numbers, achieving improvements of up to 3.8 times when the inner cylinder is eccentrically positioned at the bottom. At higher Rayleigh numbers, natural convection dominates and vibration has minimal effect. Furthermore, Majdi et al. [14] examined natural convection in a horizontal concentric ring and concluded that the radius ratio and Rayleigh number strongly influence heat transfer, whereas the inclination angle has little impact.

Additional insight was provided by Horimek et al. [15], who performed computational studies of natural convection between two concentric ellipses under fifty configurations with two heating conditions. Their research highlighted the influence of Rayleigh number, aspect ratio and orientation on flow dynamics, temperature distributions and average Nusselt number, demonstrating that geometry substantially affects heat transfer and thermal uniformity. Moreover, Laidoudi et al. [16] and Mohammed [17] showed that varying the inclination angle of non-circular inner tubes, such as elliptical or triangular shapes, can also influence heat transfer efficiency.

In recent decades, numerous strategies have been proposed to improve heat transfer performance, particularly for natural convection systems. Effective approaches include the use of cavities filled with porous media, which alter fluid flow and thermal characteristics through their permeability and porosity, as well as the application of magnetic fields to control the flow. For instance, Abdullah et al. [18] analysed natural convection within a vertical porous annulus, while Azzouz et al. [19] studied the effect of magnetic forces on natural convection in a circular enclosure containing four internal cylinders, emphasising their relevance to thermal performance. Wang et al. [20] demonstrated that, in a radiative magnetohydrodynamic natural convection system within a horizontal annulus, the magnetic field suppresses fluid motion and heat transfer, whereas radiation and fluid optical properties modify flow patterns and reduce angular variations in heat transfer.

Nanofluids, with their superior thermal conductivity and favourable rheological properties, have emerged as promising fluids for enhancing heat transfer, improving both energy transport and flow characteristics compared with conventional fluids [21]. Abdullah et al. [22] conducted computational modelling of natural convection in an inclined annular enclosure filled with an aluminium oxide-water nanofluid using the stream function-vorticity method, showing that heat transfer is affected by the Rayleigh number, inclination angle and nanoparticle volume fraction. Joby et al. [23] reviewed the effects of internal object geometry and enclosure tilt on natural convection in rectangular enclosures, emphasising the roles of Rayleigh number, nanoparticles, and porous media while noting that most previous studies were numerical, laminar and simplified, limiting their practical applicability. Other relevant studies include Mahdy et al. [24], who investigated magneto-natural convection of a micropolar hybrid nanofluid over a vertical plate in a porous medium; Payam et al. [25], who examined the influence of heat source eccentricity on entropy generation and natural convection of a copper-water nanofluid within a porous annulus; and Allouche et al. [26], who used silver-magnesium oxide nanofluid in a ring-shaped cavity considering radiation and heat absorption/generation, employing the finite volume method with the Gauss-Seidel approach. Bouzerzour et al. [27] studied a confocal elliptical annulus filled with a silver-water nanofluid, while Ali et al. [28] investigated an egg-shaped porous copper nanofluid enclosure with an internal cylindrical object using the finite element method based on the Galerkin approach. Tayebi et al. [29] examined magnetohydrodynamic natural convection in a circular annulus filled with a carbon nanotube-based nanofluid containing a heat-generating solid cylinder.

Phase change materials are acknowledged for their ability to reduce energy consumption and improve thermal storage capabilities; however, their limited thermal conductivity constrains overall effectiveness. Nano-encapsulated phase change materials address this limitation by enhancing thermo-physical properties, expediting thermal responses and facilitating integration with cooling systems, photovoltaic modules and energy storage devices, as demonstrated by Mebarek-Oudina et al. [30]. Alomari et al. [31] demonstrated that the Rayleigh number, NEPCM concentration and the orientation of the magnetic field significantly affect heat transfer in cavities composed of oscillating fins. Conversely, the paper [32] indicated that magnetic fields may decrease heat transfer by as much as 25.9%, even in the presence of enhancements from nanoparticles and elevated Rayleigh numbers. Rashid et al. [33] conducted a review on heat transfer across different cavity geometries utilising phase change materials and non-equilibrium phase change materials. Additionally, Abderrahmane et al. [34] showed that an increase in Rayleigh and Darcy numbers within a porous, magnetised inverse T-shaped enclosure leads to a notable enhancement in the average Nusselt number. Mehryan et al. [35] observed that within eccentric annuli, a particle concentration of 5% optimises heat transfer, while variations in eccentricity or cylinder elevation lead to a decrease in efficiency. Ghalambaz et al. [36] investigated NEPCM suspensions within eccentric annular geometries, demonstrating improved thermal performance through mechanisms of absorption, storage and release, with optimal fusion temperatures varying according to the Rayleigh number. Furthermore, the paper [37] illustrated that NEPCM suspensions incorporating eccentric copper foam within shell-and-tube configurations enhance thermal storage efficiency.

The latest advances involve the studies of Hussain et al. [38], who investigated the phenomenon of magneto-bioconvection in non-Newtonian electro-rheological phase change materials within H-type cavities populated by oxytactic microorganisms. Their research elucidates the influence of various parameters, including cavity aspect ratio, Darcy and Hartmann numbers, as well as Rayleigh and bioconvection Rayleigh numbers, on the dynamics of flow and thermal characteristics. Their research demonstrated that an elevated cavity aspect ratio improves the performance, whereas higher Hartmann numbers diminish nanofluid velocity and the distribution of microorganisms, with artificial neural networks (ANNs) effectively forecasting critical parameters. El Shehabey et al. [39] utilised incompressible smoothed particle hydrodynamics to investigate thermosolutal convection of NEPCM suspensions within a Bezier annulus. Their findings indicate that the Frank-Kamenetskii number, Soret-Dufour effects, Rayleigh number and nanoparticle fraction have a substantial impact on the temperature, velocity and performance of NEPCM. Additionally, artificial neural networks (ANNs) demonstrated efficacy in predicting average Nusselt and Sherwood numbers. The findings from these studies indicate that NEPCMs, when integrated with sophisticated cavity geometries, magnetic fields, bioconvection effects and computational intelligence tools, present significant opportunities for enhancing heat transfer and thermal energy storage in intricate systems.

Considering the existing literature, ring-shaped cavities featuring diverse inner cylinder shapes (circular, triangular, square) have been thoroughly examined regarding their implications for natural convection heat transfer, particularly in relation to contemporary manufacturing systems. Despite the existence of various studies on this subject, there is a scarcity of comprehensive analysis regarding the mixtures of water-based nano-encapsulated phase change materials within an annular space that includes an internally shaped cylinder. This study seeks to address the existing gap by analysing enclosures featuring an elliptical inner cylinder positioned at various inclination angles with the intention of providing more guidance to industrial manufacturers in optimising configurations that improve heat transfer rates and minimise potential discrepancies in thermal performance. The present research examines the occurrence of laminar natural convection heat transfer taking place within an eccentric circular cavity, which is cooled at its outer boundary and contains a heated inner cylinder created by the orthogonal intersection of two similar elliptical cylinders. The annular space includes a porous medium and is subjected to a magnetic force. The host fluid is comprised of water and nano-encapsulated phase change material. This research investigates the influence of various parameters including the Rayleigh number (10^3–10^6), Hartmann number (0–80), Darcy number (10^{-5}–10^{-2}), nanoparticle volume fraction (0–5%), and inclination angle (0–80°). The analysis fo-

cuses on the average Nusselt number, flow structures, temperature distribution and heat capacity ratio.

2. Problem formulation

As shown in Fig. 1, the problem under study is a 2d ring-shaped hollow comprising two elliptical cylinders of identical size crossing perpendicularly to form a concentric inner cylinder. The outer space is a circular enclosure sustained at a cold temperature T_c, designated by its radius r, whereas the interior cylinder is regarded as warmer at a temperature T_h ($T_h > T_c$).

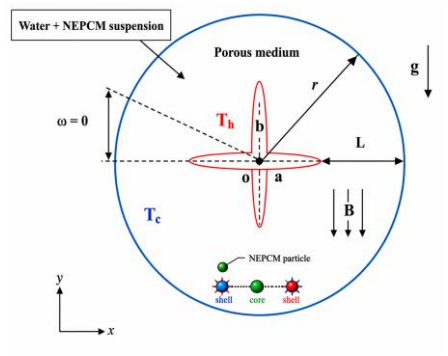


Fig. 1. Representation of the physical problem.

Table 1. Thermo-physical properties of the working fluid [35,40].

Material	P (kg/m³)	β (×10⁻⁵ K⁻¹)	C_p (kJ/(kg K))	K (W/(m K))
Water base: fluid	997.1	21	4.179	0.613
Nonadecane: core	721	–	2.037	–
Polyurethane: shell	786	17.28	1.3177	–

The elliptical section is geometrically represented by the aspect ratio, defined as the ratio of the semi-minor axis b to the semi-major axis a ($H = b/a = 0.1$). The radial gap between the exterior and interior cylinders is delineated by ($L = r - a$). The radii ratio, known as the ratio of the semi-major axis a to the radius r of the cold space, is defined as $RR = a/r = 0.4$. The annular space is occupied by a porous medium and is affected by a magnetic force. The elliptical cylinder is slanted at an angle ω that fluctuates between 0° to 80°. The injected fluid is a combination of pure water and nano-encapsulated PCM, regarded as an incompressible and Newtonian fluid. An NEPCM is formed of a PCM core, which is nonadecane and a polyurethane encapsulating shell developed from polymeric ingredients to guarantee thermal stability and prevent leakage.

The Boussinesq approximation is employed to deal with the thermal buoyancy force brought about by vertical temperature gradients. The analysis aims to assess the influence of several fundamental governing and geometrical parameters on the flow behaviour, thermal patterns, and heat capacity ratio. Namely, the inclination angle, Darcy number, Rayleigh number, Hartmann number, as well as the volume fraction ratio and the Nusselt number. Thermo-physical features of the working fluid are presented in Table 1.

3. The governing equations

This inquiry pertains to laminar and stationary flow. The fundamental equations of continuity, momentum, and energy are resolved in two dimensions within the framework of the Cartesian coordinate system. Consequently, the governing equations can be outlined as [34,35,37,38]:

$$\frac{\partial u}{\partial x} + \frac{\partial v}{\partial y} = 0, \tag{1}$$

$$\frac{\rho_b}{\varepsilon^2}\left(u\frac{\partial u}{\partial x} + v\frac{\partial u}{\partial y}\right) = -\frac{\partial p}{\partial x} + \frac{\mu_b}{\varepsilon}\nabla^2 \mathrm{u} - \frac{\mu_b}{K_0}u, \tag{2a}$$

$$\frac{\rho_b}{\varepsilon^2}\left(u\frac{\partial v}{\partial x} + v\frac{\partial v}{\partial y}\right) = -\frac{\partial p}{\partial y} + \frac{\mu_b}{\varepsilon}\nabla^2 \mathrm{v} + \beta_b \rho_b g(T - T_c) + -\frac{\mu_b}{K_0} - \frac{\sigma B_0^2}{\rho}v, \tag{2b}$$

$$\left(\rho C_p\right)_b\left(u\frac{\partial T}{\partial x} + v\frac{\partial T}{\partial y}\right) = k_b \nabla^2 T, \tag{3}$$

where u and v denote the velocity components in both x- and y-axes, respectively. P indicates the pressure, whereas T stands for the temperature.

Boundary conditions

The boundary conditions for heat transfer and fluid flow are defined in accordance with the schematic model laid out in Fig. 1:

at the cold boundary (cylinder):

$$u = v = 0 \text{ and } T = T_c, \tag{4a}$$

at the hot boundary:

$$u = v = 0 \text{ and } T = T_h. \tag{4b}$$

The suspension's bulk features:

The expression that follows provides the global density of the NEPCM mixture:

$$\rho_b = (1 - \phi)\rho_f + \phi\rho_p. \tag{5}$$

However, the density of the nanoparticles is:

$$\rho_b = \frac{(1+\iota)\rho_{co}\rho_{sh}}{\iota\rho_{co} + \rho_{sh}}. \tag{6}$$

The notations f, p, co, sh characterise the base fluid, added nanoparticles, the core and the shell, while ρ_f, ρ_p, ρ_{co}, ρ_{sh} and ι are the host fluid density, the additional nanoparticle density, the core and shell densities, and the mass ratio of the shell and core constituents, given by ι~0.447, respectively. In addition, ϕ denotes the concentration of the NEPCM particles [35,40].

Also, the density of the PCM core is found by averaging the densities of its liquid and solid forms. Upon incorporating the NEPCM into the water-based suspension, and based on the energy equation, the specific heat capacity of the suspension is ascertained as being:

$$C_{p,b} = \frac{(1-\phi)(\rho C_p)_f + \phi(\rho C_p)_p}{\rho_p}. \quad (7)$$

At the lack of phase change, the heat capacity of an encapsulated nanoparticle is expressed as:

$$C_{p,p} = \frac{(C_{p,co} + \iota C_{p,sh})\rho_{co}\rho_{sh}}{(\rho_{sh} + \iota\rho_{co})\rho_p}. \quad (8)$$

The internal material, often designated as the core, can be represented by calculating the average of the specific heat capacities of its solid and liquid states. This methodology elucidates the role of latent heat during phase transitions in influencing the effective heat capacity of the NEPCM, without considering the state of the nanoparticle core, whether it be solid or liquid. The latent heat associated with phase transitions can be integrated into the specific heat of the core by employing various profiles, including rectangular, triangular, or sinusoidal functions – Eqs. (9)–(11). The enhanced formulation for thermal capacity is presented as follows [40]:

$$C_{p,p} = vC_{p,co} + \frac{h_{sf}}{T_{Mr}}, \quad (9)$$

$$c_{p,p} = c_{p,co} + \left\{\frac{\pi}{2}\left(\frac{h_{sf}}{T_{Mr}} - C_{p,co}\right)\sin\left(\pi\frac{T - T_{fu} + (T_{Mr}/2)}{T_{Mr}}\right)\right\}, \quad (10)$$

$$C_{p,p} = C_{p,co} + 2\left(\frac{h_{sf}}{T_{Mr}^2} - \frac{C_{p,co}}{T_{Mr}}\right)(T - T_{fu}). \quad (11)$$

Most of researchers use a simplified method to deal with the problems, such as the linear interpolation. In this work, the sinusoidal function – Eq. (10) – is employed to maintain numerical convergence. T_{Mr} in this instance signifies the temperature band which involves the phase alteration. To prevent the energy equilibrium from becoming erratic, this discrepancy is intended. The aggregate specific heat capacity of the nanoparticle's core is determined by the function T_{Mr}, which entails both sensible and latent heat contributions. In this case, the phase transition occurs over a finite temperature range centred at the fusion temperature T_{fu} with a melting-range width of T_{Mr}.

$$uc_{p,p} = c_{p,co} + \left\{\frac{\pi}{2}\left(\frac{h_{sf}}{T_{Mr}} - c_{p,co}\right)\sin\left(\pi\frac{T - T_{fu} + (T_{Mr}/2)}{T_{Mr}}\right)\right\}\begin{Bmatrix} 0,\ T < T_{fu} - \frac{T_{Mr}}{2} \\ 1, T_{fu} - \frac{T_{Mr}}{2} < T < T_{fu} + \frac{T_{Mr}}{2} \\ 0,\ T > T_{fu} + \frac{T_{Mr}}{2} \end{Bmatrix}. \quad (12)$$

The volumetric thermal expansion of the mixture is estimated by the formula:

$$\beta_b = (1-\phi)\beta_f + \phi\beta_p. \quad (13)$$

Furthermore, the dynamic viscosity and thermal conductivity of a solution containing nano-encapsulated particles have been widely investigated by different scientists. As a result, these quantities are determined via linear expressions [40]:

$$\frac{k_b}{k_f} = 1 + \phi N_c, \quad (14)$$

$$\frac{\mu_b}{\mu_f} = 1 + \phi N_v. \quad (15)$$

The preceding formulas indicate that N_c and N_v stand for thermal conductivity and dynamic viscosity enhancement factors, respectively. In a mixture with nanoparticles, higher values of these parameters enhance the effective thermal conductivity and dynamic viscosity. In several types of nanofluids and hybrid nanofluids, Ghalambaz et al. [40] implemented set values for N_c and N_v that were compatible for $\phi < 5\%$, which is a specific nanoparticle volume fractional percentage [40]; the values taken in this study are $N_c = N_v = 3$ [40–43].

The governing equations in non-dimensional form:

The following variables are introduced to alter the governing equations and the boundary conditions into a non-dimensional form:

$$X = \frac{\bar{x}}{L},\ Y = \frac{\bar{y}}{L},\ RR = \frac{a}{r},\ P = \frac{\bar{p}L^2}{\rho_f\alpha_f^2},\ \theta = \frac{T - T_c}{\Delta T},$$

$$L = r - a,\ \alpha_f = \frac{k_f}{(\rho c_p)_f},\ U = \frac{\bar{u}L}{\alpha_f},\ V = \frac{\bar{v}L}{\alpha_f}. \quad (16)$$

where $\Delta T = T_h - T_c$.

The dimensionless key parameters that govern the natural convection heat transfer in a porous medium with a magnetic field are represented by the Rayleigh number 'Ra', Prandtl number 'Pr', Darcy number 'Da', and Hartmann number 'Ha' are also introduced:

$$\mathrm{Ha} = B_0 L\sqrt{\frac{\sigma_f}{\mu_f}}, \quad (17)$$

$$\mathrm{Ra} = \frac{g\rho_f\beta_f\Delta T L^3}{\alpha_f\mu_f}, \quad (18)$$

$$\mathrm{Pr} = \frac{\mu_f}{\alpha_f\rho_f}, \quad (19)$$

$$\mathrm{Da} = \frac{K_0}{L^2}. \quad (20)$$

The set of governing equations (1)–(3) can then be converted into the following set of non-dimensional equations:

$$\frac{\partial U}{\partial X} + \frac{\partial V}{\partial Y} = 0, \quad (21)$$

$$\varepsilon^{-2}\left(\frac{\rho_b}{\rho_f}\right)\left(U\frac{\partial U}{\partial X} + V\frac{\partial U}{\partial Y}\right) = -\frac{\partial P}{\partial X} + \mathrm{Pr}\,\varepsilon^{-1}\left(\frac{\mu_b}{\mu_f}\right)\nabla^2 U - \frac{\mathrm{Pr}}{\mathrm{Da}}\left(\frac{\mu_b}{\mu_f}\right)U, \quad (22a)$$

$$\varepsilon^{-2}\left(\frac{\rho_b}{\rho_f}\right)\left(U\frac{\partial V}{\partial X} + V\frac{\partial V}{\partial Y}\right) = -\frac{\partial P}{\partial Y} + \mathrm{Pr}\,\varepsilon^{-1}\left(\frac{\mu_b}{\mu_f}\right)\nabla^2 V + \left(\frac{\beta_b}{\beta_f}\right)\mathrm{Ra}\,\mathrm{Pr}\,\theta - \mathrm{Ha}^2\,V - \frac{\mathrm{Pr}}{\mathrm{Da}}\left(\frac{\mu_b}{\mu_f}\right)V, \quad (22b)$$

$$\frac{(\rho C_p)_b}{(\rho C_p)_f}\left(U\frac{\partial\theta}{\partial X}+V\frac{\partial\theta}{\partial Y}\right)=\left(\frac{k_b}{k_f}\right)\nabla^2\theta, \tag{23}$$

with

$$\left(\frac{\rho_b}{\rho_f}\right)=(1-\phi)+\phi\left(\frac{\rho_p}{\rho_f}\right), \tag{24}$$

$$\left(\frac{\beta_b}{\beta_f}\right)=(1-\phi)+\phi\left(\frac{\beta_p}{\beta_f}\right). \tag{25}$$

It is postulated that NEPCM particles expand in a manner that is identical to that of the host fluid, water, due to the absence of a slip mechanism between the base fluid and NEPCMs. Thus, the thermal expansion ratio is approximately $\beta_p/\beta_f \sim 1$.

The relative heat capacity of the basic fluid and the suspension Cr can be found via [40]:

$$\mathrm{Cr}=\frac{(\rho C_p)_b}{(\rho C_p)_f}=(1-\phi)+\phi\lambda+\frac{\phi}{\delta\mathrm{Ste}}f. \tag{26}$$

The sensible heat capacity ratio λ, Stefan number Ste, the dimensionless melting interval Θ, and fusion parameter f are established as [35,40]:

$$\lambda=\frac{(C_{p,co}+\iota C_{p,sh})\rho_{co}\rho_{sh}}{(\rho C_p)_f(\iota\rho_{co}+\rho_{sh})}, \tag{27}$$

$$\mathrm{Ste}=\frac{(\rho C_p)_f(T_h-T_c)(\iota\rho_{co}+\rho_{sh})}{\alpha_f(h_{sf}\,\rho_{co}\,\rho_{sh})}, \tag{28},$$

$$\Theta=\frac{T_{Mr}}{\Delta T}=\frac{T_{Mr}}{T_h-T_c}, \tag{29}$$

$$f=\frac{\pi}{2}\sin\left(\frac{\pi}{\theta}\left(\theta-\theta_{fu}+\frac{\Theta}{2}\right)\right)\begin{cases}0,\ \theta<\theta_{fu}-\frac{\Theta}{2}\\ 1,\theta_{fu}-\frac{\Theta}{2}<\ \theta<\theta_{fu}+\frac{\Theta}{2}\\ 0,\ \theta>\theta_{fu}+\frac{\Theta}{2}\end{cases} \tag{30}$$

This leads to the identification of the non-dimensional temperature of fusion θ_{fu} as:

$$\theta_{fu}=\frac{T_{fu}-T_c}{T_h-T_c}. \tag{31}$$

The final form of the derived governing equations is as follows:

$$\frac{\partial U}{\partial X}+\frac{\partial V}{\partial Y}=0, \tag{32}$$

$$\varepsilon^{-2}\left((1-\phi)+\phi\frac{\rho_b}{\rho_f}\right)\left(U\frac{\partial U}{\partial X}+V\frac{\partial U}{\partial Y}\right)=-\frac{\partial P}{\partial X}+\mathrm{Pr}\,\varepsilon^{-1}(1+\phi N_v)\nabla^2U-\frac{\mathrm{Pr}}{\mathrm{Da}}(1+\phi N_v)U, \tag{33a}$$

$$\varepsilon^{-2}\left((1-\phi)+\phi\frac{\rho_b}{\rho_f}\right)\left(U\frac{\partial V}{\partial X}+V\frac{\partial V}{\partial Y}\right)=-\frac{\partial P}{\partial Y}+\mathrm{Pr}\,\varepsilon^{-1}(1+\phi N_v)\nabla^2V+\left((1-\phi)+\phi\left(\frac{\beta_p}{\beta_f}\right)\right)\mathrm{Ra}\,\mathrm{Pr}\,\theta-\mathrm{Ha}^2V-\frac{\mathrm{Pr}}{\mathrm{Da}}(1+\phi N_v)V, \tag{33b}$$

$$\left((1-\phi)+\phi\lambda+\frac{\phi}{\delta\mathrm{Ste}}f\right)\left(U\frac{\partial\theta}{\partial X}+V\frac{\partial\theta}{\partial Y}\right)=(1+\phi N_c)\nabla^2\theta. \tag{34}$$

Boundary conditions in dimensionless form

The non-dimensional model of the boundary conditions can be formulated as:

at the cold wall (cylinder):

$$U=V \text{ and } \theta=0, \tag{35a}$$

at the hot cylinder:

$$U=V \text{ and } \theta=1. \tag{35b}$$

The foregoing equation describes the local heat transfer across the heated wall:

$$\mathrm{Nu}=-(1+\phi N_c)\frac{\partial\theta}{\partial Y}. \tag{36}$$

The overall heat transfer rate is determined from the integration of the earlier developed mathematical expressions:

$$\overline{\mathrm{Nu}}=\frac{1}{2\pi}\int_0^{2\pi}\mathrm{Nu}\,\mathrm{d}Y. \tag{37}$$

4. Computational procedure

The fundamental equations can be resolved using several approaches. In the investigated problem, the Galerkin weighted residual finite element method is employed to streamline the computing procedure.

This method converts the differential equations governing the heat transfer and fluids motion into algebraic formulas that can be numerically solved. For the discretisation of the non-dimensional governing equations, a non-uniform triangular mesh is employed. A damped Newton technique with a minimum damping factor of 10^{-6} is utilised to solve the coupled momentum and energy equations, and the Galerkin approach is applied for handling the residuals. The PARDISO direct solver is implemented to improve numerical stability during matrix factorisation by incorporating a pivot perturbation value of 10^{-8}. The convergence criterion for the modelling process is determined by the tolerances defined by the solver. The relative tolerance is fixed at 10^{-6}, ensuring that the solution was deemed converged when the relative change between successive iterations fell below 0.1%.

A grid resolution analysis was conducted to verify the mesh independence of the outcomes, utilising the average Nusselt number as the reference parameter. Table 2 presents a summary of the results corresponding to different mesh densities: fine, finer, extra fine and extremely fine. The distinction between the extra fine and extremely fine meshes is barely noticeable. ΔNu is approximately 0.0193, suggesting that the solution has effect-

Table 2. Discretisation sensitivity analysis for Ra = 10^5, Ha = 0, ω = 0, ϕ = 5%.

Mesh size	Number of elements	Average Nusselt number	CPU time (s)
Fine	9640	7.1929	14
Finer	18174	7.2786	37
Extra fine	32896	7.2950	58
Extremely fine	88746	7.3143	137

tively reached convergence. Despite the increased computational time associated with the extremely fine mesh, which is 137 s in contrast to 58 s for the extra fine mesh, it is selected for all subsequent simulations. This choice ensures mesh independency and highly accurate outcomes, capturing all flow, thermal gradients, along with fluctuations in the optimal heat capacity ratio.

The typical quantities of the non-dimensional variables are established as follows: Ste = 0.313, λ = 0.4, Pr = 6.2, ρ_p / ρ_f = 0.9, θ_{fu} = 0.3, T_{Mr} = 0.05, and $N_c = N_v$ =3.

The numerical model underwent additional validation through a comparative analysis with benchmark data provided by Ghalambaz et al. [40]. Average Nusselt numbers were computed for Rayleigh numbers with ϕ = 0 and Pr = 0.7, and the findings were compared with the reference values. The data presented in Table 3 indicate a high level of concordance with the benchmark, demonstrating a maximum relative error of 0.04% across all examined cases. The robust quantitative correlation validates the precision of the governing equations, the models of material properties, and the suitability of the existing computational framework for parametric analysis.

Finally, the precision and reliability of the proposed framework were verified by comparing the streamline, temperature and Cr ratio with those reported by Ghalambaz et al. [40], as illustrated in Fig. 2. The close agreement demonstrates the robustness of the numerical model and validates its use for the sensitivity and parametric studies.

Table 3. Comparison of the mean Nusselt number at the hot wall with values published in [40] under the conditions of ϕ = 0 and Pr = 0.7.

Ra	Nu average [40]	Nu average (Present study)	Relative error (%)
10^3	1.1174	1.1178	0.0358
10^4	2.2441	2.2443	0.0089
10^5	4.5174	4.5182	0.0177
10^6	8.8167	8.8188	0.0238

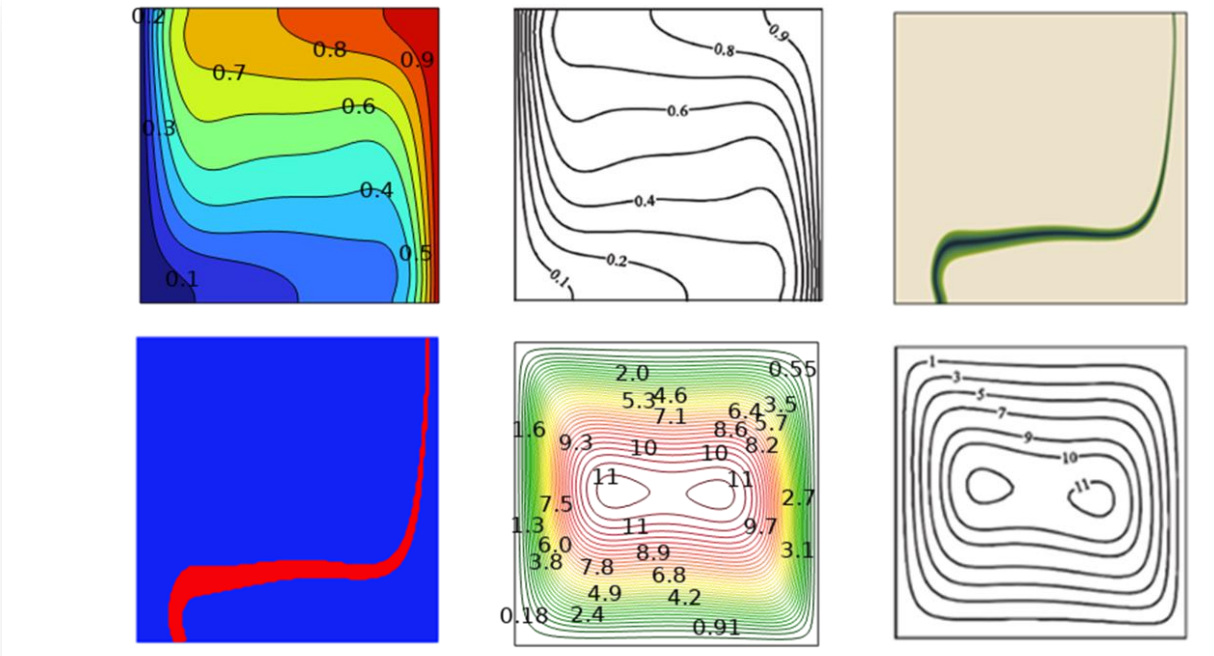


Fig. 2. Comparison of the present results (temperature, heat capacity and streamline contours, from left to right) with those of Ghalambaz et al. [40] placed on the right-side for Ra = 10^5, Ha = 0, Pr = 6.2, ω = 0°.

5. Results and discussion

In the first place, it is apparent that all contours (streamlines, isotherms and heat capacity ratio) exhibit an axisymmetric pattern along the *y*-axis for all the cases studied.

5.1. Effect of Rayleigh number for ω = 0°

Figure 3 demonstrates the significance of varied Rayleigh number values (Ra = 10^3–10^6) on streamline contours of fluid flow, thermal features and heat capacity ratio, considering Ha = 0, ϕ = 0.05, Pr = 6.2, and Da = 10^{-2} at a constant inclination angle of $\omega = 0^{\circ}$.

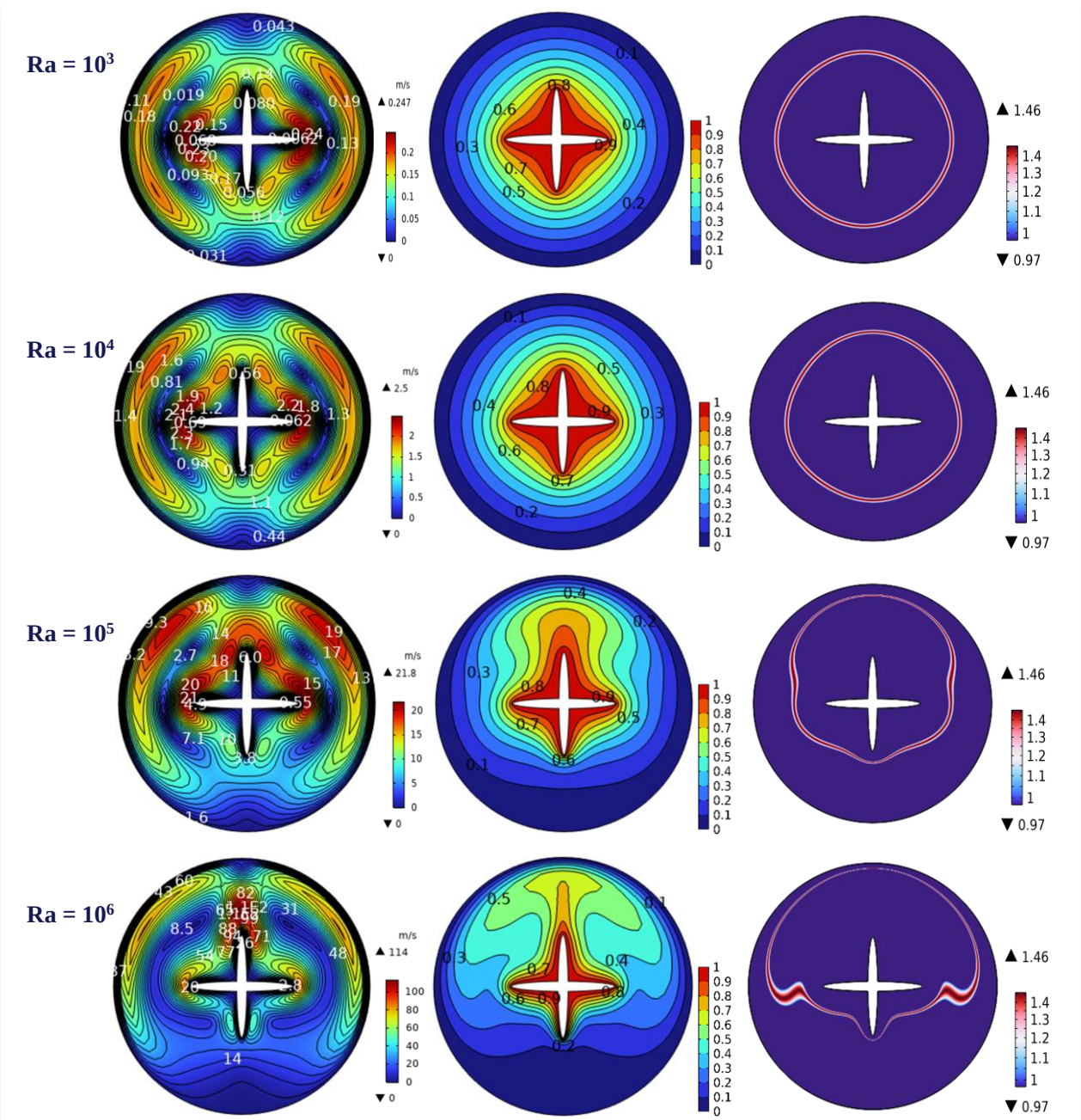


Fig. 3. Rayleigh number influence on streamline patterns (left), temperature (centre) and heat capacity ratio (right) for Ha = 0, ϕ = 0.05, Pr = 6.2 and Da = 10^{-2}. Streamlines show an increase in maximum velocity from 0.0247 m/s (Ra = 10^3) to 114 m/s (Ra = 10^6), while isotherms vary in the range 0–1.

The fluid flow profile exhibits a marked intensification of motion, especially in the regions adjacent to the hot and cold sides of the cylinders. As the Rayleigh number increases, the velocity within the annular space rises significantly, causing the flow to extend upward along the wall boundaries. Near the upper portion of the heated cylinder, the velocity reaches its maximum at Ra = 10^6 due to the dominance of convective heat transfer. The thermal distribution pattern shows a gradual temperature rise from the heated cylinder toward the cooler one. The increase in Ra further amplifies this effect, as the hot fluid migrates toward the cold region, leading the warmer, lighter fluid to ascend and the cooler, denser fluid to descend in response to the thermal gradient. At Ra = 10^6, the temperature field develops a characteristic mushroom-shaped layer that expands progressively. This behaviour reflects the mechanism of thermal buoyancy, wherein fluid near the hot surface becomes less dense and rises, while fluid near the cold surface gains density and sinks. The Cr ratio layer forms a closed circular contour around the heated cylinder, marking the region where the phase transition occurs within the cavity. Increasing the dimensionless parameter distorts this contour, causing it to widen along the lateral sides while narrowing near the cold wall and the lower section of the heated area. The resulting slender shape of the layer delineates the most favourable region for phase-change heat transfer to take place.

5.2. Effect of the Hartmann number for $\omega = 0°$

Figure 4 depicts the effect of increasing Hartmann number on the flow field, temperature distribution and heat capacity ratio for Ra = 10^6, $\phi = 0.05$, Pr = 6.2 and Da = 10^{-2} at a fixed inclination angle $\omega = 0^{\circ}$.

The streamline contours show that increasing the magnetic field intensity (Hartmann number) leads to a reduction in the overall flow rate due to the Lorentz force, which acts as a resistive mechanism opposing fluid motion. The isotherms indicate a more uniform temperature distribution under stronger magnetic effects. The heat capacity ratio contours exhibit a mushroom-shaped layer surrounding the heated cylinder, characterised by thicker lateral regions that narrow towards both the lower part of the hot boundary and the vicinity of the cold wall. As the non-dimensional parameter increases, this pattern shows no deformation.

5.3. Darcy number impact for $\omega = 0°$

Figure 5 presents the permeability influence in the porous medium cavity denoted by the Darcy number at Ra = 10^6, $\phi = 0.05$, Pr = 6.2, and Da = 10^{-2} at a fixed inclination angle $\omega = 0^{\circ}$.

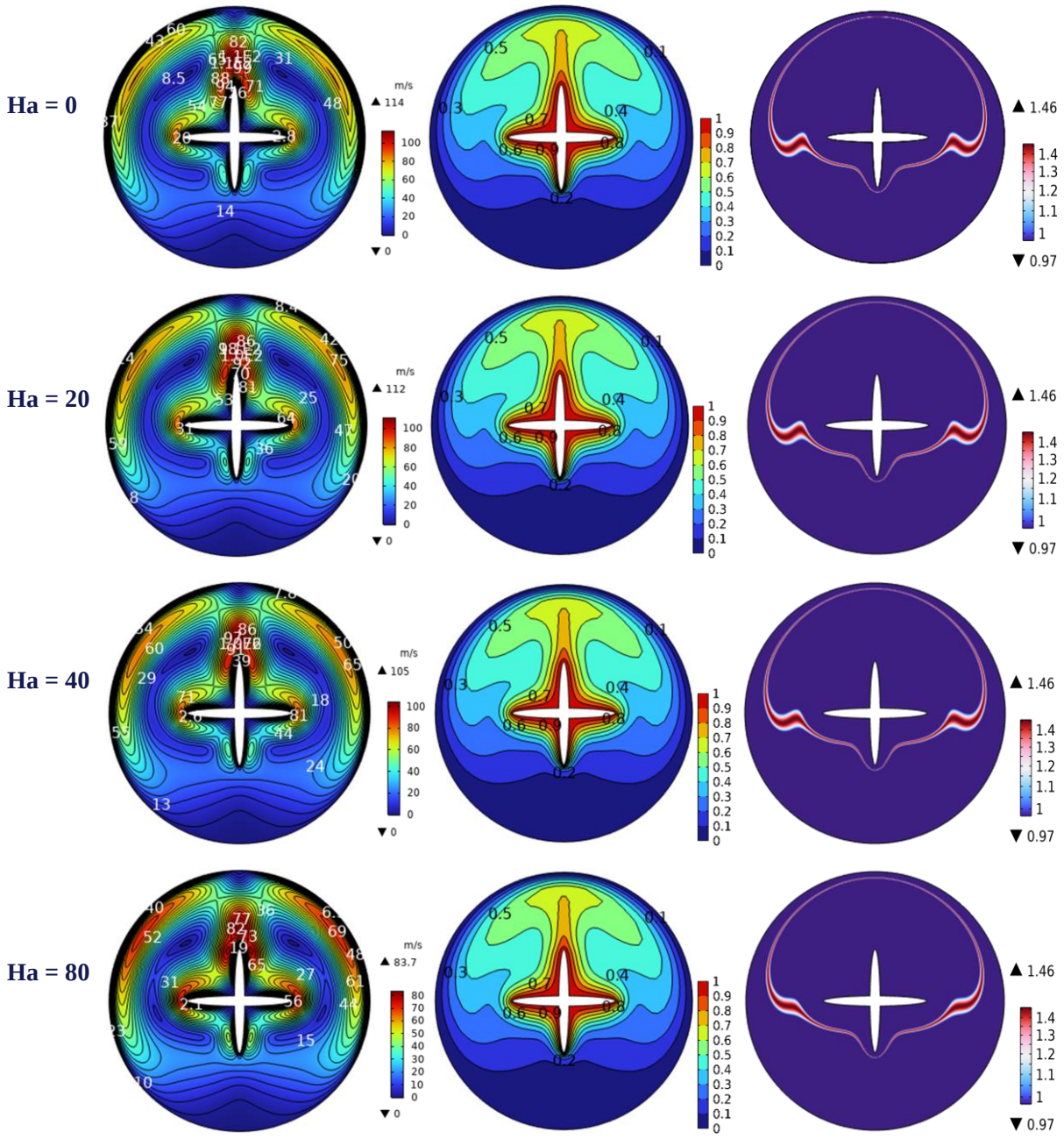


Fig. 4. Hartmann number influence on streamline patterns (left), temperature (centre) and heat capacity ratio (right) for Ra = 10^6, $\phi = 0.05$, Pr = 6.2 and Da = 10^{-2}. Streamlines show a decrease in maximum velocity from 114 m/s (Ha = 0) to 83.7 m/s (higher Ha), while isotherms vary in the range 0–1.

The velocity contours reveal that increasing the Darcy number promotes stronger fluid movement inside the enclosure, particularly around the extremities of the lateral edges of the heated cylinder, its upper section and along the cold boundary.

The thermal field displays an initially uniform distribution from the hot region to the cold region; as the Darcy number rises, this distribution expands outward and develops into a mushroom-shaped thermal layer.

The heat capacity ratio contours exhibit a curved boundary encircling the heated obstacle. As the dimensionless parameter increases, this boundary undergoes noticeable deformation: it becomes thinner near the cold wall and in the lower part of the hot boundary, while the lateral regions expand and become comparatively thicker.

5.4. The influence of inclination angle ω (10°, 30°, 60°, and 80°) on the streamlines, isotherms and Cr patterns

Figures 6, 7, and 8 designate the streamlines, isotherms and Cr contours, respectively, at multiple degrees of inclination angle and Ra number with Ha = 0, ϕ = 0.05, Pr = 6.2 and Da = 10^{-2}.

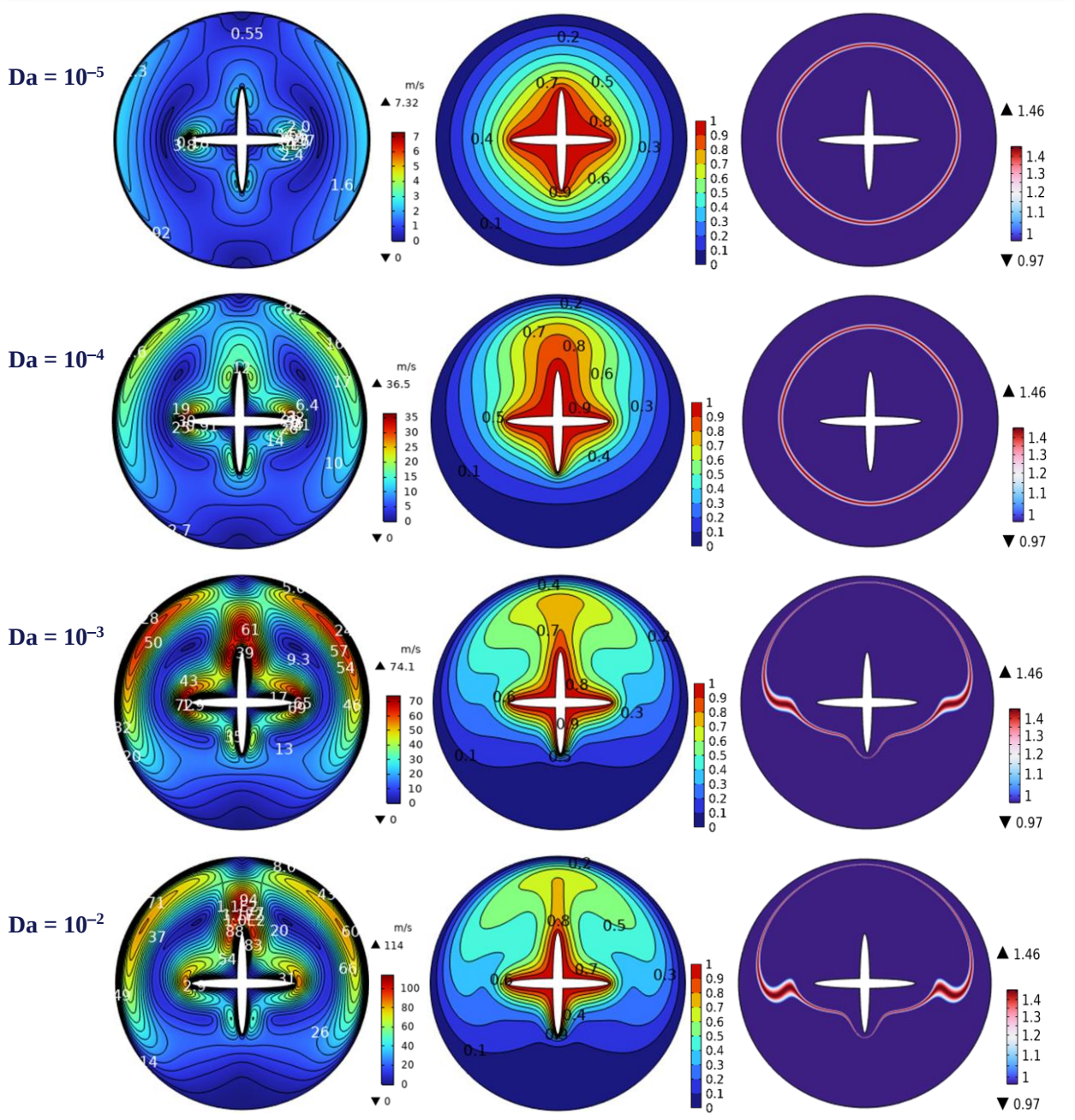


Fig. 5. Darcy number influence on velocity (left), temperature (centre) and heat capacity ratio (right) for Ha = 0, ϕ =0.05, Pr = 6.2 and Ra = 10^6. Streamlines show an increase in maximum velocity from 7.32 m/s (Da = 10^{-5}) to 114 m/s (Da = 10^{-2}), while isotherms vary in the range 0–1.

As observed, the inclination angle ω exerts a significant influence on the streamlines, isotherms and Cr ratio patterns. Notably, an inclination of 10° behaves as the angular counterpart of 80°, while 30° mirrors 60°.

The streamline patterns indicate that the velocity reaches its maximum near the corners of the inner cylinder and along the sidewalls of the outer enclosure, generating concentrated velocity zones on both the left and right sides. Increasing both the Rayleigh number and the inclination angle enhances the fluid motion, causing the flow to accelerate and extend upward across the upper region of the annular domain.

Figure 7 illustrates the thermal field, where the temperature is the highest near the heated surface and gradually diffuses towards the cooler region. The rise in Rayleigh number facilitates the upward migration of heat within the cavity, producing a mushroom-shaped isotherm pattern. As the inclination angle increases, the heat distribution expands, resulting in a more pronounced deformation of this mushroom-like structure.

Figure 8 displays the heat capacity ratio, characterised by a thick, curved boundary surrounding the heated cylinder. For inclination angles of 10° and 80°, increasing the Rayleigh number causes this boundary to bend outward, becoming broader along the lateral sides while narrowing near the upper region of the outer cylinder and the lower region adjacent to the heated surface at Ra = 10^6. Additionally, a semi-circular line emerges near the lower wing of the cavity. A similar behaviour is ob-

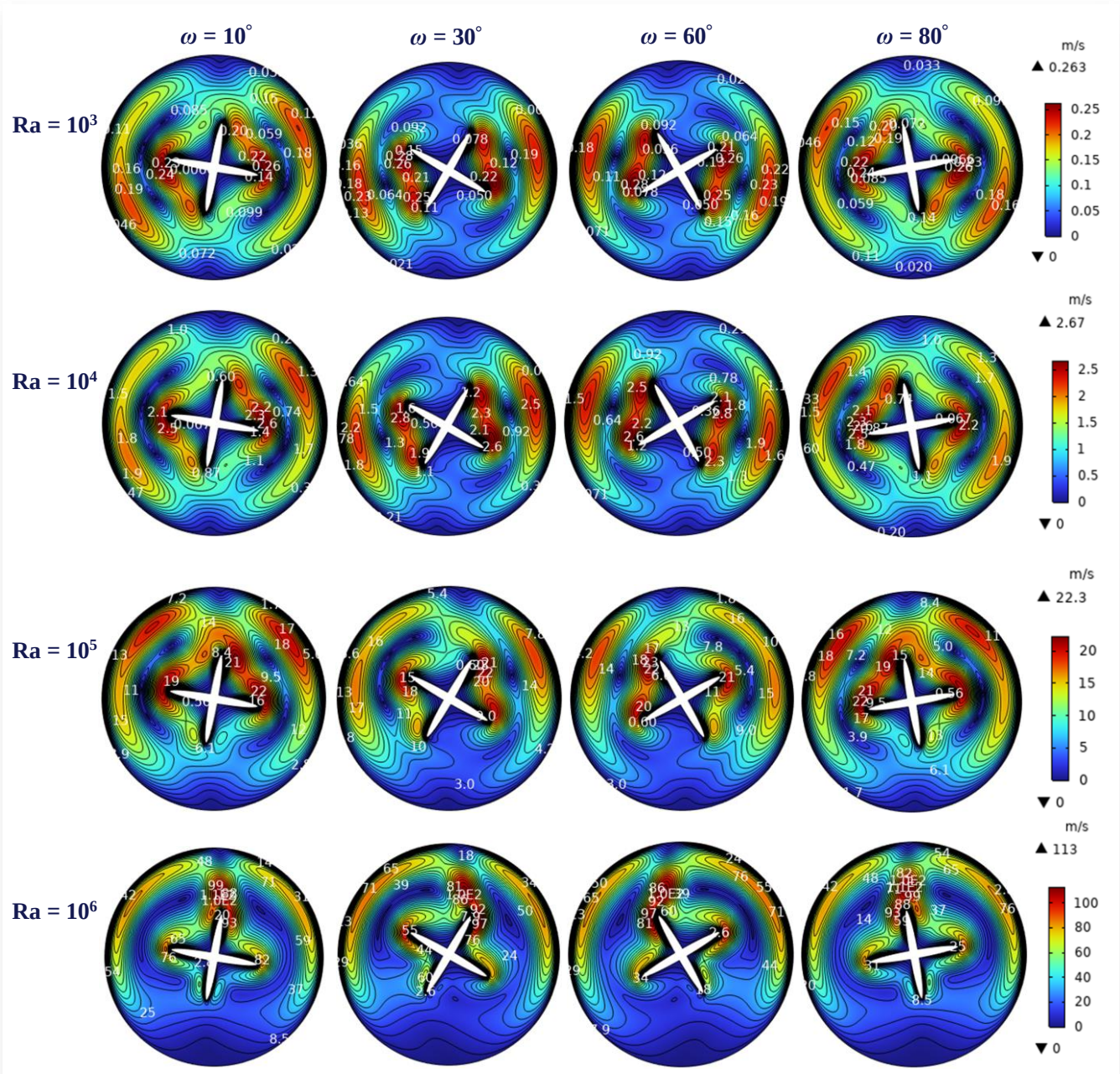


Fig. 6. Streamlines for various values of inclination angle (ω =10º, 30º, 60º, 80º, respectively) and Ra number for Ha = 0, ϕ =0.05, Pr = 6.2 and Da = 10^{-2}. The maximum velocity increases from 0.263 m/s (Ra = 10^3) to 113 m/s (Ra = 10^6).

served for inclination angles of 30° and 60°, although the pattern more closely resembles a mushroom-like contour enveloping the hot boundary.

5.5. Average Nusselt number influence

Figure 9 presents variations of the average Nusselt number with the Rayleigh number (10^3–10^6) for different Hartmann numbers (0–20), Darcy numbers (10^{-5}–10^{-2}), NEPCM volume fractions (0%–5 %), and inclination angles (10°–80°).

Figure 9a shows that the Nusselt number decreases as both the Hartmann and Rayleigh numbers increase. This reduction is attributed to the resistive action of the Lorentz force, which suppresses fluid motion and consequently slows the heat transfer rate within the cavity.

Figure 9a illustrates a direct correlation between the Darcy and Rayleigh numbers, demonstrating that an increase in the Rayleigh number leads to a corresponding rise in the Darcy number. As the Darcy number increases, the permeability of the porous medium improves, enhancing convective heat transfer and resulting in a higher Nusselt number.

Figure 9a demonstrates that the increasing NEPCM volume fraction (0–0.05) augments the thermal storage capacity of the suspension. This behaviour confirms a direct proportionality between the Rayleigh number and the NEPCM concentration, enabling more efficient heat transport and producing higher Nusselt number values.

Figure 9d highlights the influence of the inclination angle, showing that its increase leads to larger Rayleigh number values. Unlike the previous cases, increasing the inclination angle from 0° to 30° results in a reduction of the Nusselt number, indicating diminished heat transfer. In contrast, for inclination angles between 60° and 80°, the Nusselt number rises significantly, indicating an enhancement of heat transfer across the annular region.

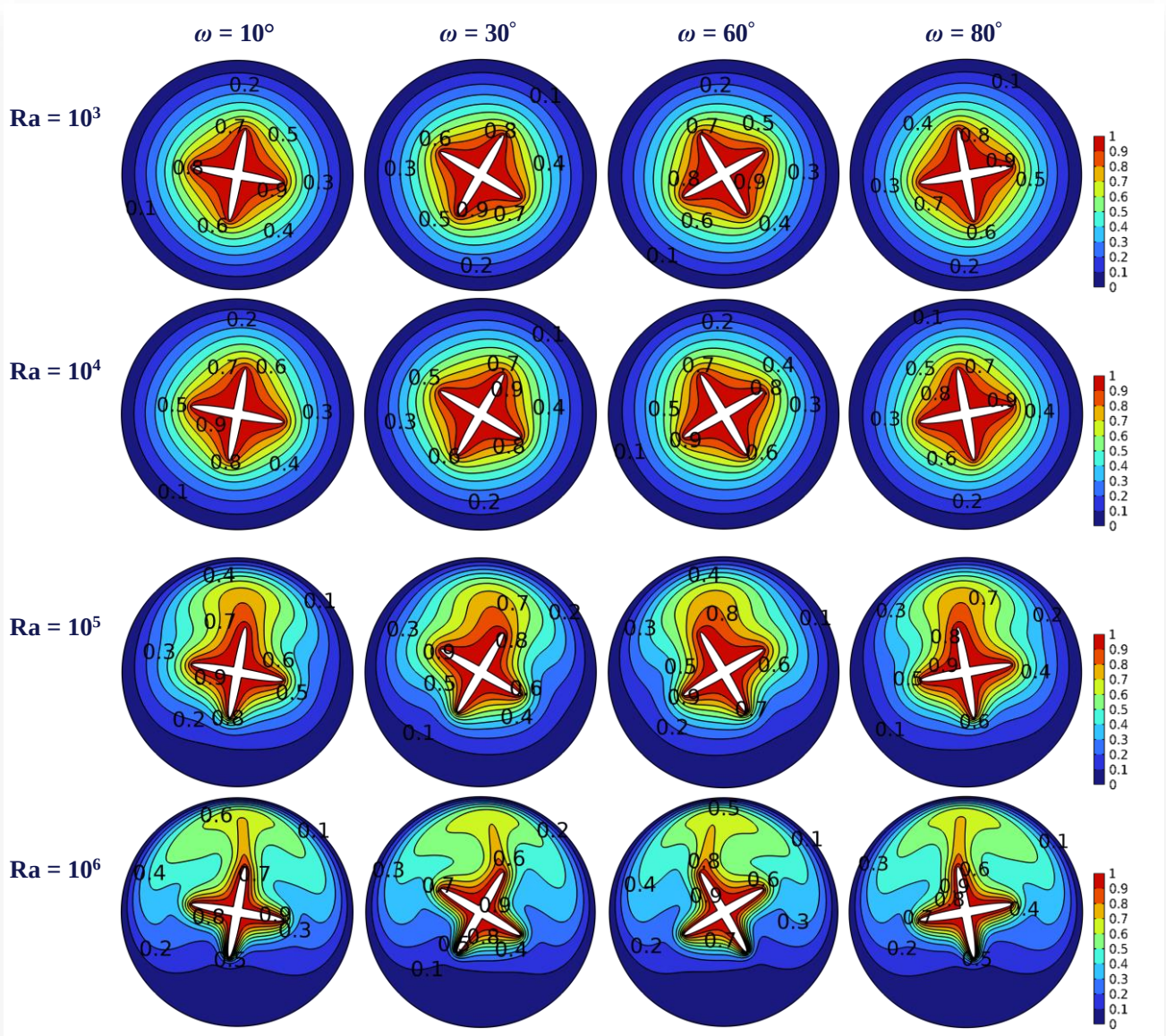


Fig. 7. Isotherms for various values of inclination angle (ω = 10°, 30°, 60°, 80°, respectively) and Ra number for Ha = 0, ϕ = 0.05, Pr = 6.2 and Da = 10^{-2}.

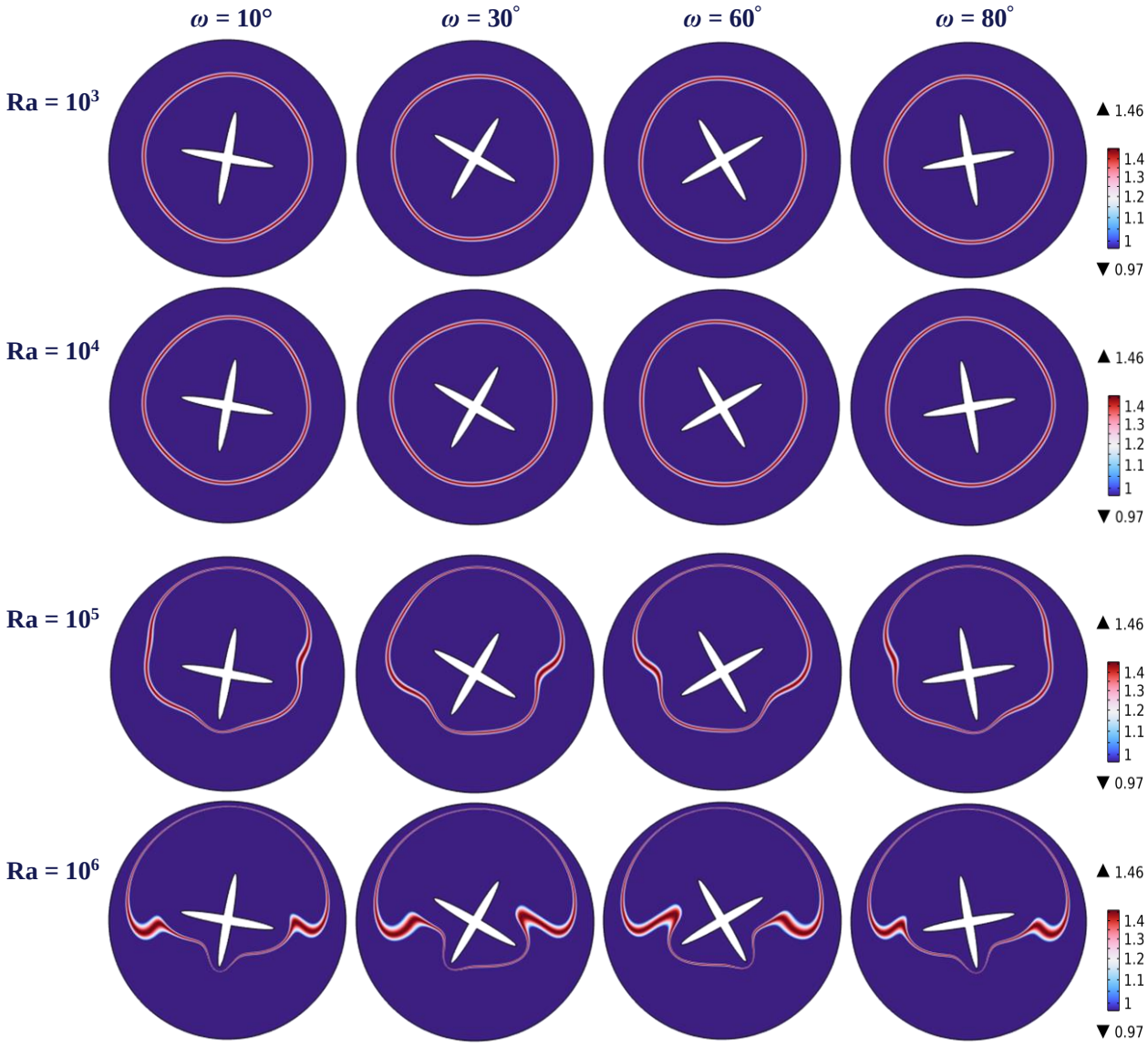


Fig. 8. Heat capacity ratio patterns for various values of inclination angle (ω = 10º, 30º, 60º, 80º) and Rayleigh number for Ha = 0, ϕ = 0.05, Pr = 6.2 and Da = 10^{-2}.

The Nusselt number trends indicate that configurations with inclination angles between 0° and 30° are better suited for thermal insulation applications, as they promote energy efficiency and help preserve temperature differences. Conversely, inclination angles ranging from 60° to 80° are more advantageous for processes requiring intensified heat transfer.

6. Conclusions

The presented work undertakes a numerical analysis of a two-dimensional annular space comprising a cold outer cylinder and a hot inner obstacle generated through the overlap of two congruent elliptical cylinders. The aspect ratio of the overlapping cylinders is 0.1, and the radii ratio between the annular spaces is 0.4.

The suspension incorporated is NEPCM, which is a composite nanofluid developed by suspending nano-encapsulated phase change materials in pure water. The enclosure is porous and subject to the influence of a magnetic field. This study investigates the effects of several dimensionless parameters on streamline patterns, isotherms and the heat capacity ratio (Cr). The parameters considered are the Rayleigh number (10^3–10^6), Darcy number (10^{-5}–10^{-2}) and Hartmann number (0–80), along with the inclination angle of the intersecting inner cylinders ω (0°–80°). The results also highlight the practical implementation of these geometries in contemporary applications.

At ω = 0°, the fields of velocity, temperature, and concentration ratio exhibit symmetry throughout the annular space. The flow velocity is particularly high along the lateral sides of the

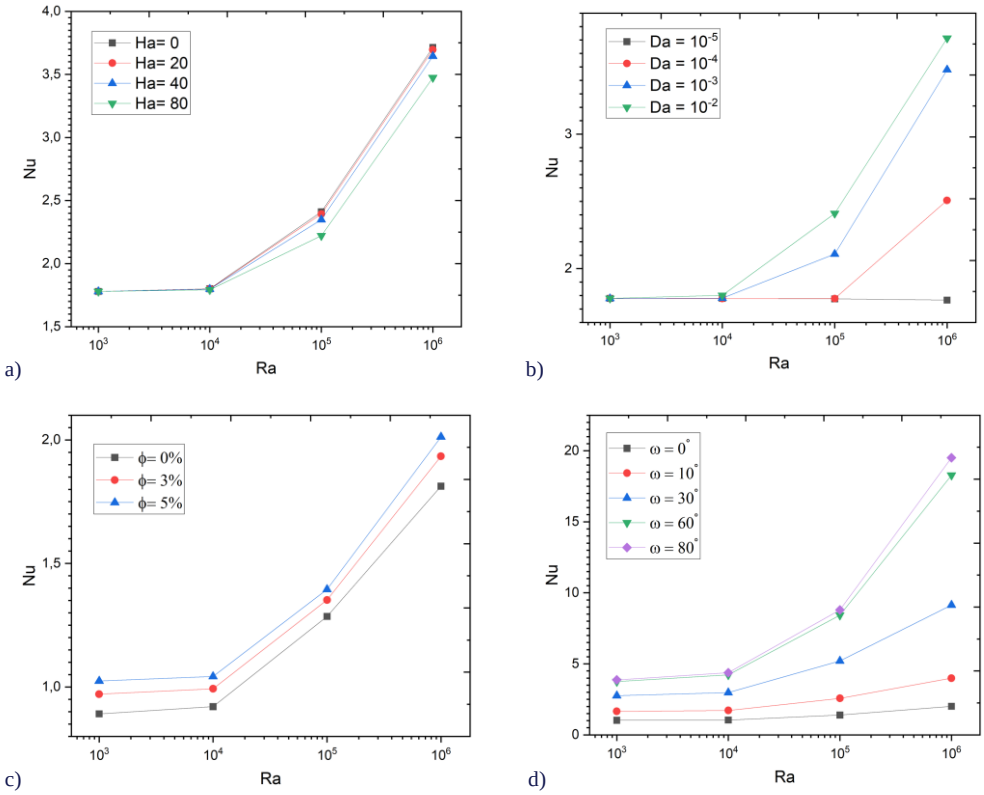


Fig. 9. Average Nusselt number as a function of Rayleigh number for different values of Hartmann number (a), Darcy number (b), NEPCM volume fraction (c), and inclination angle (d).

inner cylinder and near the sidewall of the outer enclosure. Increasing the Rayleigh and Darcy numbers strengthens the vortices and promotes stronger convective currents. This intensification enhances the temperature gradients, increases the heat transfer rate and modifies the spatial distribution of the NEPCM effective heat capacity, with higher values becoming concentrated near the boundary regions and extending along the sidewalls.

Additionally, the Lorentz forces generated by the magnetic field significantly affect the flow, reducing convective velocities as the Hartmann number increases. This leads to weakened vortices, a uniform nanoparticle distribution and a decrease in the average Nusselt number, reflecting a reduced heat transfer intensity, while the inclination angle ω directly influences the level of imbalance and asymmetry of the flow rate, thermal gradient and Cr patterns.

Lastly, the changes in the average Nusselt number with regard to Ra, Da, Ha, ϕ and ω are provided to shed light on their relevance in specific sectors of industry. For instance, inclination angles ranging from 0° to 30° signify that the configuration performs as an insulator due to slower heat transfer rates, in contrast to angles between 60° and 80°, which are more beneficial to heat transfer enhancement.

References

[1] Li, C., Zhao, Z., Liu, X., & Ding, J. (2023). Numerical study of the effect of natural convection on heat transfer in type B LNG cargo tank. *International Joint Conference on Civil and Marine Engineering* (pp. 499–502), 3–6 November, Dalian, China. doi: 10.1049/icp.2024.0263

[2] Dirkse, M.H., van Loon, W.K., van der Walle, T., Speetjens, S.L., & Bot, G.P. (2006). A computational fluid dynamics model for designing heat exchangers based on natural convection. *Biosystems Engineering*, 94(3), 443–452. doi: 10.1016/j.biosystemseng.2006.04.007

[3] Phiraphat, S., Prommas, R., & Puangsombut, W. (2017). Experimental study of natural convection in PV roof solar collector. *International Communications in Heat and Mass Transfer*, 89, 31–38. doi: 10.1016/j.icheatmasstransfer.2017.09.022

[4] Zhang, G., Jiang, S., Yao, W., & Liu, C. (2016). Enhancement of natural convection by carbon nanotube films covered microchannel-surface for passive electronic cooling devices. *ACS Applied Materials & Interfaces*, 8(45), 31202–31211. doi: 10.1021/acsami.6b08815

[5] Laguerre, O., & Flick, D. (2004). Heat transfer by natural convection in domestic refrigerators. *Journal of Food Engineering*, 62(1), 79–88. doi: 10.1016/S0260-8774(03)00173-0

[6] Kuehn, T.H., & Goldstein, R.J. (1978). An experimental study of natural convection heat transfer in concentric and eccentric horizontal cylindrical annuli. *ASME Journal of Heat and Mass Transfer*, 100(4), 635–640. doi: 10.1115/1.3450869

[7] Wang, S. (1995). An experimental and numerical study of natural convection heat transfer in horizontal annuli between eccentric cylinders. *Journal of Thermal Science*, 4(1), 38–43. doi: 10.1007/BF02653162

[8] Laidoudi, H. (2020). Natural convection from four circular cylinders in across arrangement within horizontal annular space. *Acta Mechanica et Automatica*, 14(2), 98–102. doi: 10.2478/ama-2020-0014

[9] Laidoudi, H. (2020). Buoyancy-driven flow in annular space from two circular cylinders in tandem arrangement. *Metallurgical and Materials Engineering*, 26(1), 87–102. doi: 10.30544/481

[10] Laidoudi, H., & Ameur, H. (2021). Investigation of the natural convection within a cold circular enclosure containing three equal-sized cylinders of hot surface. *Defect and Diffusion Forum*, 409, 49–57. doi: 10.4028/www.scientific.net/ddf.409.49

[11] Laidoudi, H., Ameur, H., Sahebi, S.A.R., & Hoseinzadeh, S. (2022). Thermal analysis of steady simulation of free convection from concentric elliptical annuli of a horizontal arrangement. *Arabian Journal for Science and Engineering*, 47(12), 15647–15660. doi: 10.1007/s13369-022-06717-5

[12] Helmaoui, M., Laidoudi, H., Ghenaim, A. (2021). Natural convection from two hot semi-circular cylinders confined in cold circular cylinder. *Defect and Diffusion Forum*, 409, 58–66. doi: 10.4028/www.scientific.net/ddf.409.58

[13] Khudhair, B.K., Saleh, A.M., & Ekaid, A.L. (2023). Influence of vertical vibration on natural heat convection coefficients. *Pertanika Journal of Science and Technology*, 31(3), 1555–1586. doi: 10.47836/pjst.31.3.24

[14] Majdi, H.S., Habeeb, L.J., Elmnifi, M., & Alderoubi, N. (2022). Transient free convection between two horizontal concentric cylinders. *International Journal of Mechanical Engineering*, 7(1), 596–609.

[15] Horimek, A., Abdelmoumene, F., & Ait Messaoudene, N. (2023). Numerical Study of Natural Convection between Two Concentric Ellipses with Different Shapes and Imposed Temperatures. *Mechanical Engineering Technologies and Applications*, 2, 105–128. doi: 10.2174/9789815124125123020l

[16] Laidoudi, H., Helmaoui, M., Bouzit, M., & Ghenaim, A. (2021). Natural convection of Newtonian fluids between two concentric cylinders of a special cross-sectional form. *Thermal Scienc*e, 25(5B), 3701–3714. doi: 10.2298/TSCI200201190L

[17] Mohammed, A.A. (2021). Natural convection heat transfer inside horizontal circular enclosure with triangular cylinder at different angles of inclination. *Journal of Thermal Engineering*, 7(1), 240–254. doi: 10.18186/thermal.849812

[18] Alguboori, A.R., Al-azzawi, M.M., Kalash, A.R., & Habeeb, L.J. (2020). Natural convection heat transfer in an inclined elliptic enclosure with circular heat source. *Journal of Mechanical Engineering Research and Developments*, 43(6), 207–222.

[19] Azzouz, R., & Hamida, M.B. (2023). Natural convection in a circular enclosure with four cylinders under magnetic field. *Processes*, 11(8), 2444. doi:10.3390/pr11082444

[20] Wang, W., Li, B.W., & Hu, Z.M. (2019). Magnetohydrodynamic natural convection in cylindrical annulus. *Journal of Heat Transfer*, 141(6), 062502. doi:10.1115/1.4042811

[21] Ali, A.R.I., & Salam, B. (2020). A review on nanofluid: preparation, stability, thermophysical properties, heat transfer characteristics and application. *SN Applied Sciences*, 2(10), 1636. doi: 10.1007/s42452-020-03427-1

[22] Mahmood, M.A., Mustafa, M.A., Al-Azzawi, M.M., & Abdullah, A.R. (2020). Natural convection heat transfer in a concentric annulus vertical cylinders embedded with porous media. *Journal of Advanced Research in Fluid Mechanics and Thermal Sciences*, 66(2), 65–83.

[23] Jobby, A., Khatamifar, M., & Lin, W. (2025). A comprehensive review on the natural convection heat transfer in horizontal and inclined closed rectangular enclosures with internal objects at various heating conditions. *Energies*, 18(4), 950. doi: 10.3390/en18040950

[24] Mahdy, A., El-Zahar, E.R., Rashad, A.M., Saad, W., & Al-Juaydi, H.S. (2021). The magneto-natural convection flow of a micropolar hybrid nanofluid over a vertical plate saturated in a porous medium. *Fluids*, 6(6), 202. doi: 10.3390/fluids6060202

[25] Gholamalipour, P., Siavashi, M., & Doranehgard, M.H. (2019). Eccentricity effects of heat source inside a porous annulus on the natural convection heat transfer and entropy generation of Cu-water nanofluid. *International Communications in Heat and Mass Transfer*, 109, 104367. doi: 10.1016/j.icheatmasstransfer.2019.104367

[26] Allouche, B., Djezzar, M., Allouche, S., & Tayebi, T. (2026). Natural convection heat transfer in an eccentric annulus filled with hybrid nanofluid under the influence of thermal radiation and heat generation/absorption. *Numerical Heat Transfer, Part A: Applications*, 87(1), 2386607. doi: 10.1080/10407782.2024.2386607

[27] Bouzerzour, A., Djezzar, M., Oztop, H.F., Tayebi, T., & Abu-Hamdeh, N. (2020). Natural convection in nanofluid filled and partially heated annulus: Effect of different arrangements of heaters. *Physica A: Statistical Mechanics and its Applications*, 538, 122479. doi: 10.1016/j.physa.2019.122479

[28] Ali, F.H., Almensoury, M.F., Hashim, A.S., Al-Amir, Q.R., Hamzah, H.K., & Hatami, M. (2024). Nanofluid natural convection of hot concentric cylinder in oval-shaped porous cavity at different eccentricity. *International Journal of Numerical Methods for Heat & Fluid Flow*, 34(5), 2146–2176. doi: 10.1108/HFF-08-2023-0494

[29] Tayebi, T., Öztop, H.F., & Chamkha, A.J. (2021). MHD natural convection of a CNT-based nanofluid-filled annular circular enclosure with inner heat-generating solid cylinder. *The European Physical Journal Plus*, 136(2), 150. doi: 10.1140/epjp/s13360-021-01106-7

[30] Mebarek-Oudina, F., & Chabani, I. (2023). Review on nano enhanced PCMs: insight on nePCM application in thermal management/storage systems. *Energies*, 16(3), 1066. doi: 10.3390/en16031066

[31] Alomari, M.A., Hassan, A.M., Alajmi, A., Sadeq, A.M., Alqurashi, F., & Flayyih, M.A. (2025). A comprehensive numerical analysis of heat transfer enhancement in NEPCM-water mixtures using oscillating fin and oriented magnetic fields. *International Communications in Heat and Mass Transfer*, 161, 108455. doi: 10.1016/j.icheatmasstransfer.2024.108455

[32] Alomari, M.A., Hassan, A.M., Sadeq, A.M., Alqurashi, F., & Flayyih, M.A. (2025). MHD Heat Transfer Enhancement in a Curvilinear Enclosure With Oscillating Wall and Nano-Encapsulated PCM: A Fluid-Structure Interaction Analysis. *Heat Transfer*, 54(6), 4049–4072. doi: 10.1002/htj.23399

[33] Rashid, F.L., Mohammed, H.I., Dulaimi, A., Al-Obaidi, M.A., Talebizadehsardari, P., Ahmad, S., & Ameen, A. (2023). Analysis of heat transfer in various cavity geometries with and without nano-enhanced phase change material: A review. *Energy Reports*, 10, 3757–3779. doi: 10.1016/j.egyr.2023.10.036

[34] Abderrahmane, A., Al-Khaleel, M., Mourad, A., Laidoudi, H., Driss, Z., Younis, O., Guedri, K., & Marzouki, R. (2022). Natural convection within inversed T-shaped enclosure filled by nano-enhanced phase change material: Numerical investigation. *Nanomaterials*, 12(17), 2917. doi: 10.3390/nano12172917

[35] Mehryan, S.A.M., Ghalambaz, M., Gargari, L.S., Hajjar, A., & Sheremet, M. (2020). Natural convection flow of a suspension containing nano-encapsulated phase change particles in an eccentric annulus. *Journal of Energy Storage*, 28, 101236. doi: 10.1016/j.est.2020.101236

[36] Ghalambaz, M., Mehryan, S.A.M., Ayoubloo, K.A., Hajjar, A., El Kadri, M., Younis, O., Pour, M.S., & Hulme-Smith, C. (2021). Thermal energy storage and heat transfer of nano-enhanced phase

change material (NePCM) in a shell and tube thermal energy storage (TES) unit with a partial layer of eccentric copper foam. *Molecules*, 26(5), 1491. doi: 10.3390/molecules26051491

[37] Ghalambaz, M., Mehryan, S.A.M., Mozaffari, M., Zadeh, S.M. H., & Pour, M.S. (2020). Study of thermal and hydrodynamic characteristics of water-nano-encapsulated phase change particles suspension in an annulus of a porous eccentric horizontal cylinder. *International Journal of Heat and Mass Transfer*, 156, 119792. doi: 10.1016/j.ijheatmasstransfer.2020.119792

[38] Hussain, S., Aly, A.M., Alsedias, N., & Çolak, A.B. (2024). Integrating artificial intelligence in investigating magneto-bioconvection flow of oxytactic microorganisms and nano-enhanced phase change material in H-type cavity. *Thermal Science and Engineering Progress*, 49, 102497. doi: 10.1016/J.TSEP.2024.102497

[39] Elshehabey, H.M., Aly, A.M., Lee, S.W., & Çolak, A.B. (2024). Integrating artificial intelligence with numerical simulations of Cattaneo-Christov heat flux on thermosolutal convection of nano-enhanced phase change materials in Bézier-annulus. *Journal of Energy Storage*, 82, 110496. doi: 10.1016/J.EST.2024.110496

[40] Ghalambaz, M., Chamkha, A.J., & Wen, D. (2019). Natural convective flow and heat transfer of nano-encapsulated phase change materials (NEPCMs) in a cavity. *International Journal of Heat and Mass Transfer*, 138, 738–749. doi: 10.1016/j.ijheatmasstransfer.2019.04.037

[41] Sheikholeslami, M., & Sadoughi, M.K. (2018). Simulation of CuO-water nanofluid heat transfer enhancement in presence of melting surface. *International Journal of Heat and Mass Transfer*, 116, 909–919. doi: 10.1016/j.ijheatmasstransfer.2017.09.086.

[42] Zaraki, A., Ghalambaz, M., Chamkha, A.J., Ghalambaz, M., & De Rossi, D. (2015). Theoretical analysis of natural convection boundary layer heat and mass transfer of nanofluids: effects of size, shape and type of nanoparticles, type of base fluid and working temperature. *Advanced Powder Technology*, 26(3), 935–946. doi : 10.1016/j.apt.2015.03.012

[43] Ghalambaz, M., Doostani, A., Izadpanahi, E., & Chamkha, A.J. (2017). Phase-change heat transfer in a cavity heated from below: the effect of utilizing single or hybrid nanoparticles as additives. *Journal of the Taiwan Institute of Chemical Engineers*, 72, 104–115. doi: 10.1016/j.jtice.2017.01.010